Materials Today Communications 43 (2025) 111670

Contents lists available at ScienceDirect

Materials Today Communications

journal homepage: www.elsevier.com/locate/mtcomm

Abnormal absorption of novel high-entropy diborides regulated by electromagnetic balance of magnetic elements

Shuyi Zeng [a], Qingyun Chen [a,*], Qijie Chen [a], Xingye Wang [b], Peng Sun [c], Chencheng Liu [b,*], Tong Zhu [b], Yi Zhu [b], Wenlong Zhang [b], Yuezhong Wang [b,*], Nan Jiang [b]

[a] College of Physics and Electronic Information Engineering, Guilin University of Technology, Guilin 541004, China
[b] State Key Laboratory of Advanced Marine Materials, Ningbo Institute of Materials Technology and Engineering, Chinese Academy of Sciences, Ningbo 315201, China
[c] Tianjin Key Laboratory of Optical Thin Films, Tianjin Jinhang Technical Physics Institute, Tianjin 300308, China

ARTICLE INFO

Keywords:
Transition metal diboride (TMB_2)
High-entropy (HE)
Electromagnetic wave absorption
Dielectric losses
Magnetic flux losses
Electromagnetic balance

ABSTRACT

The transition metal diboride (TMB_2), as an electromagnetic wave absorbing material, exhibits excellent dielectric loss properties. However, the lack of magnetic loss leads to an imbalance between dielectric loss and magnetic loss, which limits its electromagnetic wave absorption (EMA) performance. In this study, two novel high-entropy diborides $(Mo_{0.2}Zr_{0.2}V_{0.2}Nb_{0.2}X_{0.2})B_2$ (X = Ta, Fe) were successfully synthesized by a fast joule heating device for 10 minutes at 1900 °C. By introducing a magnetic element (Fe), the electromagnetic properties of the $(Mo_{0.2}Zr_{0.2}V_{0.2}Nb_{0.2}X_{0.2})B_2$ material were significantly enhanced, optimizing its electromagnetic balance and improving impedance matching. This allowed for more efficient penetration and absorption of electromagnetic waves. Moreover, the "cocktail effect" of different elements within the high-entropy system caused lattice distortion in the solid solution and the formation of defects that acted as polarization centers, further enhancing electromagnetic wave absorption. As a result, magnetic $(Mo_{0.2}Zr_{0.2}V_{0.2}Nb_{0.2}Fe_{0.2})B_2$ material demonstrated a minimum reflection loss of −31.1 dB at 15.4 GHz with a thickness of 6.0 mm, significantly lower than the −12.5 dB reflection loss at 5.7 GHz with a thickness of 5.5 mm of the non-magnetic $(Mo_{0.2}Zr_{0.2}V_{0.2}Nb_{0.2}Ta_{0.2})B_2$ materials. This significant improvement indicated its exceptional electromagnetic wave absorption properties. Related study provided a useful reference for designing high-performance electromagnetic wave absorbing materials.

1. Introduction

The swift advancement of microwave technology, coupled with the diversification of communication devices and frequency bands, has led to a notable increase in electromagnetic pollution. This phenomenon presents a considerable risk to the proper functioning of electronic equipment, the stability of digital systems, and the precision of deep space exploration endeavors [1]. Consequently, there has been a heightened emphasis on the development of absorbing materials capable of effectively capturing electromagnetic waves and converting them into heat or alternative forms of energy. In particular, the design of absorbers necessitates materials that exhibit broad bandwidth, high absorptivity, and exceptional stability [2–5].

Ceramic wave-absorbing materials, as a novel category of absorbers, exhibit considerable advantages in terms of high-temperature resistance, oxidation resistance, and resistance to acid and alkali corrosion [6,7]. Due to their distinctive properties, these ceramic absorbing materials find extensive applications in military contexts, particularly in components subjected to high temperatures, such as aircraft engine exhausts and cruise missiles, as well as in countermeasures against enemy radar detection. However, a significant challenge associated with the use of ceramic materials as wave absorbers is their tendency to exhibit poor impedance matching, primarily attributable to their intrinsic metallic conductivity. Consequently, the modulation of the electromagnetic properties of ceramic materials to facilitate the effective penetration and absorption of electromagnetic waves has emerged as a critical issue in the practical application of these materials.

Transition metal diboride (TMB_2) is a prominent constituent of the ultra-high temperature ceramics (UHTC) category, characterized by an AlB_2-type hexagonal crystal structure. This material exhibits metallic bonding among the transition metal (TM) atoms, ionic-covalent bonding between the TM and boron (B) atoms, and covalent bonding among the

* Corresponding authors.
E-mail addresses: chenqy@glut.edu.cn (Q. Chen), liuchencheng@nimte.ac.cn (C. Liu), wangyuezhong@nimte.ac.cn (Y. Wang).

https://doi.org/10.1016/j.mtcomm.2025.111670
Received 13 November 2024; Received in revised form 9 January 2025; Accepted 18 January 2025
Available online 20 January 2025

B atoms. Pan *et al.* [8,9] conducted a comprehensive analysis of the structural configuration, hardness, and thermodynamic properties of transition metal borides utilizing first-principles methods. Their findings indicate that these materials exhibit significant Vickers hardness and reveal the influence of layered structures on the thermodynamic characteristics of transition metal borides. Furthermore, Pan *et al.* [10] investigated the impact of various transition metals on the structural stability and mechanical properties of borides through first-principles calculations, concluding that the incorporation of transition metals enhances these properties. The crystal structure of TMB_2 exhibits alternating layers of graphitic boron and transition metals, with the metallic characteristics primarily arising from the d states of the transition metals and partially from the $2p_z$ states of boron [11,12]. Typically, the interaction between an incident electric field and an electric dipole results in the dissipation of electromagnetic energy, a phenomenon referred to as dielectric loss capability [13]. This capability is influenced by both conductivity loss and relaxation polarization within the gigahertz frequency range. The inherent conductivity of TMB_2 facilitates electron migration, which contributes to a decrease in electromagnetic energy manifested as conduction loss. Consequently, TMB_2 demonstrates favorable properties such as thermal stability, resistance to oxidation and corrosion, and effective dielectric loss characteristics, positioning it as a promising candidate for electromagnetic wave absorption applications. However, akin to other dielectric loss absorbers, the high conductivity of TMB_2 leads to the formation of a continuous conduction current at its surface, resulting in inadequate impedance matching and suboptimal performance in electromagnetic wave absorption [14,15].

In recent years, the advancement of high entropy ceramics (HEC) has introduced a novel approach to the design of absorbing materials. Research indicates that an increase in the configurational entropy of a system can markedly enhance the thermal stability [16], oxidation resistance [17], and corrosion resistance [18], while also allowing for effective modulation of its electrical conductivity [19,20], dielectric properties [21,22], and magnetic properties [23]. For instance, Qiao *et al.* [24] developed a high-entropy MAX phase material aimed at enhancing the wave absorption capabilities of the material, whereas Zhang *et al.* [25] optimized impedance matching by manipulating the high-entropy components, thereby altering the dielectric and magnetic losses to improve absorption performance.

Diboride ceramic materials are characterized by their high electrical conductivity, which typically results in significant dielectric loss, while magnetic loss remains comparatively minimal. This phenomenon often leads to the formation of a conductive network on the surface, causing direct reflection of incident electromagnetic waves and consequently hindering effective absorption. This process induces significant lattice distortion and local stress within the material's chemical environment, resulting in stress fluctuations. For instance, pure-phase ZrB_2 demonstrates a minimum reflection loss (RL) of no less than −5 dB within the frequency range of 1–5 mm and 2–18 GHz, with an effective absorption bandwidth (EAB) of zero [26]. Research indicates that high entropy designs present considerable potential for enhancing absorption performance and achieving impedance matching. Consequently, these effects enhance electron scattering, diminish electronic conductivity, and ultimately lead to a reduction in conductive losses [27]. In addition, a large number of defects (e.g., vacancies, interstitial atoms, etc.) in high-entropy solid solutions can act as polarization centers, which can inhibit dipole steering and space charge rearrangement under the action of an alternating electric field, thus dissipating the energy of electromagnetic waves [28]. More importantly, the introduction of magnetic components and a large number of charged defects will provide more magnetic loss pathways and enhance the magnetic loss capability [13]. For example, Zhang *et al.* [29] incorporated magnetic elements to optimize impedance matching, resulting in improved electromagnetic wave absorption. Similarly, Gao *et al.* [30] enhanced the wave absorption capabilities of composites by introducing iron, while Zhang *et al.* [31] further refined impedance matching through the incorporation of magnetic materials as a secondary phase. Therefore, by engineering high-entropy compositions, creating solid solutions of magnetic elements, stabilizing these elements within the crystal lattice, reducing the material's conductivity, and augmenting its magnetic loss capacity, it is anticipated that one can effectively regulate the electromagnetic balance and develop high-performance high-entropy ceramic materials for wave absorption.

In this study, based on high-entropy component design, two novel high-entropy diborides $(Mo_{0.2}Zr_{0.2}V_{0.2}Nb_{0.2}X_{0.2})B_2$ (X = Ta, Fe) were successfully synthesized by a fast joule heating device for 10 minutes at 1900 °C. The incorporation of the magnetic element (Fe) significantly enhanced the electromagnetic properties of the $(Mo_{0.2}Zr_{0.2}V_{0.2}Nb_{0.2}X_{0.2})B_2$ material. This enhancement is attributed to the optimization of electromagnetic equilibrium, which facilitates improved impedance matching, thereby allowing for more effective penetration and absorption of electromagnetic waves. Furthermore, the interaction among the various elements within the high-entropy system induces lattice distortions in the solid solution and generates defects that act as polarization centers within the material, further augmenting the absorption capabilities of electromagnetic waves. This study provided a valuable reference for the design and advancement of novel electromagnetic wave absorption materials.

2. Experimental

2.1. Synthesis of $(Mo_{0.2}Zr_{0.2}V_{0.2}Nb_{0.2}X_{0.2})B_2$ (X = Ta, Fe) powders

Commercially available Ta and Mo powders (purity: 99.50 %, Shanghai Aladding Biochemical Technology Co. Ltd., Shanghai, China), Fe powders (purity: 99.90 %, Shanghai Aladding Biochemical Technology Co. Ltd., Shanghai, China), Zr and powders (purity: 99.90 %, particle size: 0.2–0.4 μm, Shanghai Aladding Biochemical Technology Co. Ltd., Shanghai, China), Nb and V powders (purity: 99.99 %, Shanghai Aladding Biochemical Technology Co. Ltd., Shanghai, China) and B powders (purity: 99.90 %, Shanghai Aladding Biochemical Technology Co. Ltd., Shanghai, China) were used as the raw materials. High-entropy $(Mo_{0.2}Zr_{0.2}V_{0.2}Nb_{0.2}Ta_{0.2})B_2$ and $(Mo_{0.2}Zr_{0.2}V_{0.2}Nb_{0.2}Fe_{0.2})B_2$ powder were prepared by simple boron reduction method.

The preparation process of $(Mo_{0.2}Zr_{0.2}V_{0.2}Nb_{0.2}X_{0.2})B_2$ (X = Ta, Fe) is shown in the Fig. 1. Weigh the transition metal powders in equal moles, then mix them thoroughly with 10 % excess boron powder according to the proportions in the reaction equation [32]. Grind the mixture in an agate mortar for 2 hours to ensure sufficient contact between the raw materials and the powder. Then, press it into a bulk form at 10 MPa, which will be referred to as the precursor, ground in an agate mortar for 2 h, and in order to make the raw materials and powders fully contact, they are pressed into a block with 10 MPa, and the final block is expressed as a precursor. With a rapid joule heating device, heating at 1900 °C for 10 min, the whole heating and cooling process was carried out in flowing argon gas (purity 99.99 %) at a flow rate of 50 sccm. After natural cooling to room temperature, it is collected and ground into a fine powder.

2.2. Characterization

The phase composition of samples was analyzed by X-ray diffraction (XRD, Pert PRO), Netherlands, using Cu Kα radiation. The microstructure of as-prepared HE TMB_2 ceramic powders was investigated by a scanning electron microscopy (SEM, FEISirion 200) equipped with an energy dispersive spectroscopy (EDS). The distributions of TM elements were investigated by a transmission electron microscope (TEM, Tecnai F30G2; FEI, Eindhoven, Netherlands). Based on the transmission line theory and the metal backplate model [33], the RL is determined from the relative complex permittivity and permeability for a given frequency and sample thickness according to the following equation [34,35]:

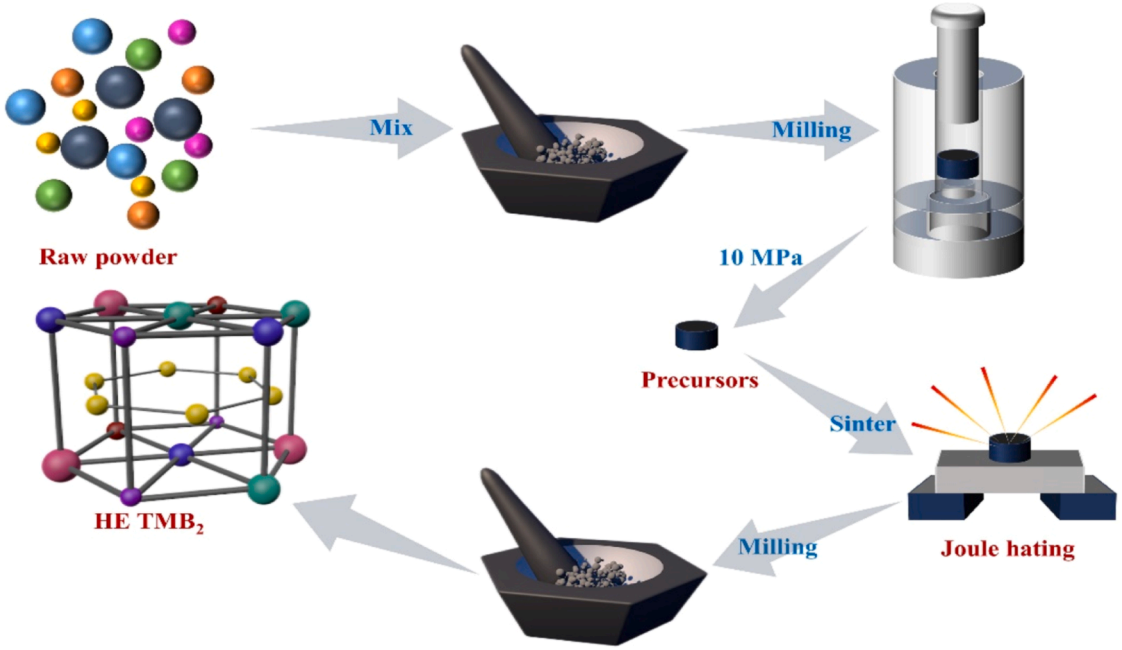

Fig. 1. The preparation process of $(Mo_{0.2}Zr_{0.2}V_{0.2}Nb_{0.2}X_{0.2})B_2$ (X = Ta, Fe).

$$RL(dB) = 20\lg\left|\frac{Z_{in} - Z_0}{Z_{in} + Z_0}\right| \quad (1)$$

$$Z_{in} = Z_0\sqrt{\frac{\mu_r}{\varepsilon_r}}\tanh\left(j\frac{2\pi fd\sqrt{\mu_r\varepsilon_r}}{c}\right) \quad (2)$$

where Z_0 is the impedance of free space, Z_{in} is the normalized input characteristic impedance at the interface between the atmosphere and the absorber, μ_r is the relative complex permeability, ε_r is the complex permittivity, f is the frequency, d is the thickness of the sample, and c is the speed of light (3×10^8 m/s). EAB is defined by a frequency range with an RL value of less than −10 dB, which corresponds to 90 % of the microwave energy absorbed [13].

3. Results and discussion

3.1. Phase composition and microstructure

Fig. 2 presents the X-ray diffraction (XRD) spectrum of the synthesized $(Mo_{0.2}Zr_{0.2}V_{0.2}Nb_{0.2}X_{0.2})B_2$ (X = Ta, Fe) powders. The primary reflection peaks are attributed to the AlB_2-type phase, which suggests that $(Mo_{0.2}Zr_{0.2}V_{0.2}Nb_{0.2}X_{0.2})B_2$ (X = Ta, Fe) powders, incorporating various transition metal (TM) elements, was successfully synthesized at a temperature of 1900 °C. The results indicate that the formation of solid solutions occurs through a multi-step process, influenced by the varying interdiffusibility of the transition metal elements [36]. Utilizing this rapid synthesis method, a pure phase of $(Mo_{0.2}Zr_{0.2}V_{0.2}Nb_{0.2}X_{0.2})B_2$ (X = Ta, Fe) was obtained, with a slight shift in the main reflection peak attributed to the presence of different solid solution TM elements and their respective atomic radii. The successful synthesis of $(Mo_{0.2}Zr_{0.2}V_{0.2}Nb_{0.2}X_{0.2})B_2$ (X = Ta, Fe) powders demonstrates the feasibility of incorporation magnetic elements into high-entropy diboride.

Fig. 3(a-f) show a representative SEM analysis of as-synthesis $(Mo_{0.2}Zr_{0.2}V_{0.2}Nb_{0.2}X_{0.2})B_2$ (X = Ta, Fe) powders. Tabular and columnar particles with residual development steps are frequently seen under various growth circumstances [37]. The morphology of the synthesized $(Mo_{0.2}Zr_{0.2}V_{0.2}Nb_{0.2}Fe_{0.2})B_2$ powder is depicted in Fig. 3(a-c). It is evident that the powder is uniformly distributed and has a porous

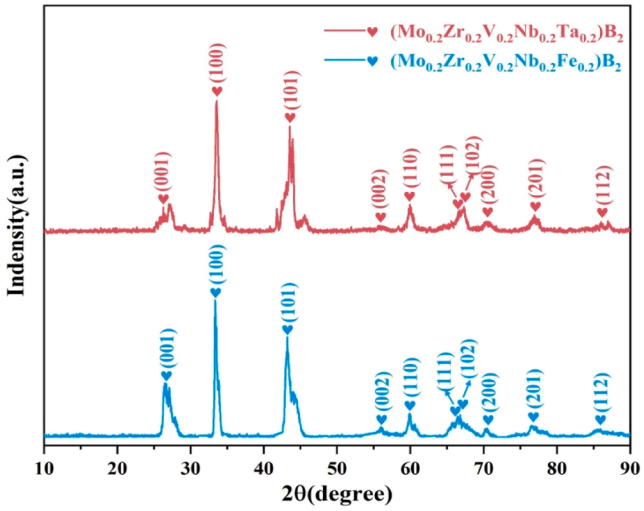

Fig. 2. XRD patterns of $(Mo_{0.2}Zr_{0.2}V_{0.2}Nb_{0.2}Ta_{0.2})B_2$ and $(Mo_{0.2}Zr_{0.2}V_{0.2}Nb_{0.2}Fe_{0.2})B_2$ synthesized at 1900 ℃ for dwelling time of 10 min.

structure, which helps to structurally enhance the dissipation of electromagnetic waves by reflecting them inside the material. The morphology of the synthesized $(Mo_{0.2}Zr_{0.2}V_{0.2}Nb_{0.2}Fe_{0.2})B_2$ powder is depicted in Fig. 3(e-f). Structural variations resulting from cocktail effects and lattice distortions attributable to disparities in high-entropy components. At the nanoscale, a clear layered structure can be observed, possibly due to the presence of nanoscale translucent sheet-like Fe_3O_4 within the crystal structure, which randomly occupies the interior of the crystal and creates gaps between the materials. It is clear that a layered structure is seen on top of the pore structure, which is anticipated to show stronger interfacial polarization and help to increase the dielectric loss.

Fig. 4(a-b) show a typical dark-field TEM image of the as-synthesized sample. It can be clearly seen that the as-synthesized sample is nanocrystalline particles and layered structure. From the selected region electron diffraction (SAED) in Fig. 4(c), it can be seen that the as-

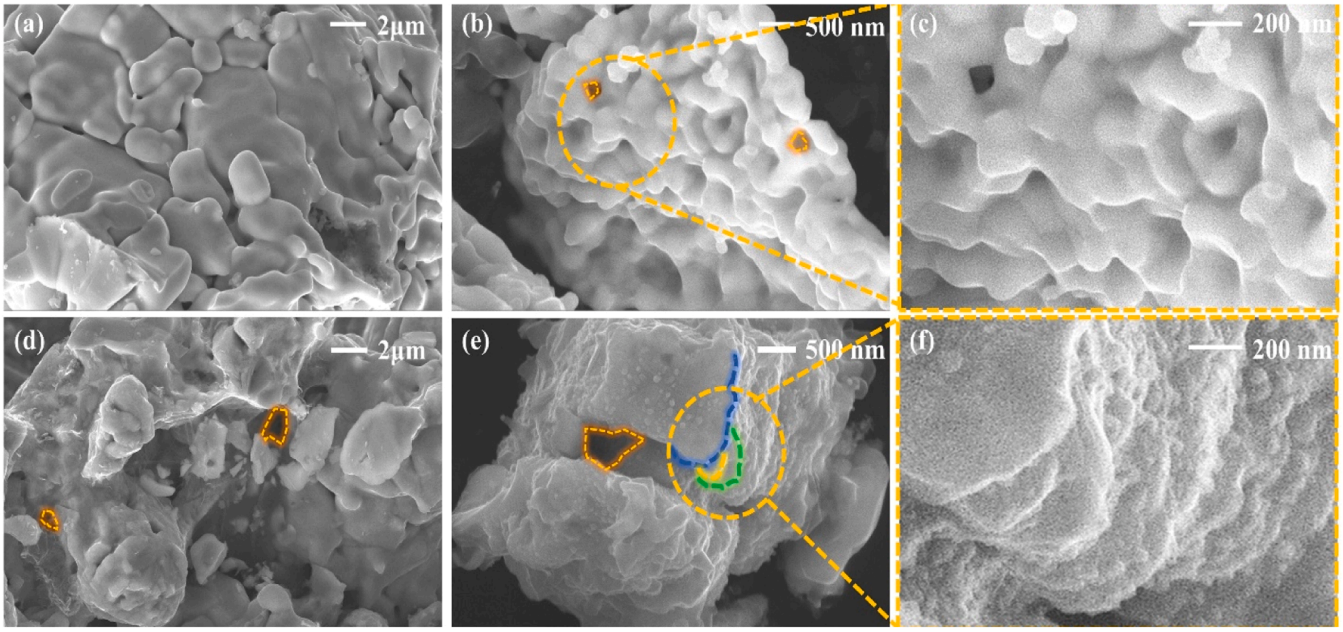

Fig. 3. SEM images of (a-c) $(Mo_{0.2}Zr_{0.2}V_{0.2}Nb_{0.2}Ta_{0.2})B_2$ and (d-f) $(Mo_{0.2}Zr_{0.2}V_{0.2}Nb_{0.2}Fe_{0.2})B_2$.

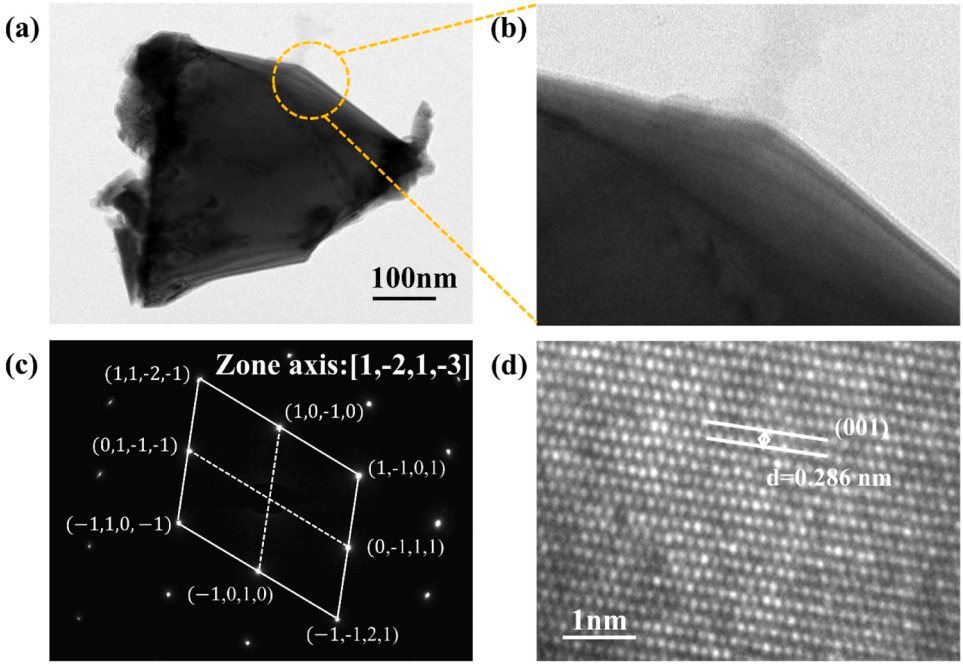

Fig. 4. (a-b) TEM image, (c) SAED pattern, and (d) HRTEM image of $(Mo_{0.2}Zr_{0.2}V_{0.2}Nb_{0.2}Fe_{0.2})B_2$.

synthesized sample has good crystallinity and symmetrically arranged diffraction patterns, exhibiting a typical AlB_2 hexagonal structure, which is consistent with the XRD results. As shown in Fig. 4(d), the surface spacing of the synthesized $(Mo_{0.2}Zr_{0.2}V_{0.2}Nb_{0.2}Fe_{0.2})B_2$ (100) is 0.286 nm. The difference in surface spacing may be caused by solid solutions of transition metal ions of different sizes in the new high-entropy system. Fig. 5 displays a representative STEM-EDS study of $(Mo_{0.2}Zr_{0.2}V_{0.2}Nb_{0.2}Fe_{0.2})B_2$ to describe the distribution of various TM elements. EDS elemental atlas Fig. 5(b) and (d) confirmed that the TM cations were distributed uniformly throughout the grain. It is possible to conclude that a single-phase HEB_2 powder with a homogeneous elemental distribution was synthesized when combined with XRD and STEM-EDS studies.

Fig. 6(a-f) plots the high-resolution XPS spectra of Mo 3d, Nb 3d, V 2p, Zr 3d, Fe 2p, and B 1 s, revealing the presence of Mo-B (231.11 and 230.68 eV for Mo $3d_{5/2}$ and Mo $3d_{3/2}$, respectively), Nb-B (205.71 eV and 208.69 eV for Nb $3d_{5/2}$ and Nb$3d_{3/2}$, respectively), and V-B (529.7 and 531.5 eV for V $2p_{3/2}$ and V $2p_{1/2}$, respectively), Zr-B (181.742 and 181.17 eV for Zr $3d_{5/2}$ and Zr $3d_{3/2}$, respectively), and Fe-B (722.46 and 708.75 eV, respectively, for Fe $2p_{3/2}$ and Fe $2p_{1/2}$, respectively) species. The X-ray photoelectron spectroscopy (XPS) results validated the synthesis of the high-entropy phase $(Mo_{0.2}Zr_{0.2}V_{0.2}Nb_{0.2}Fe_{0.2})B_2$.

3.2. *Electromagnetic properties*

The principle of electromagnetic wave absorption can be described

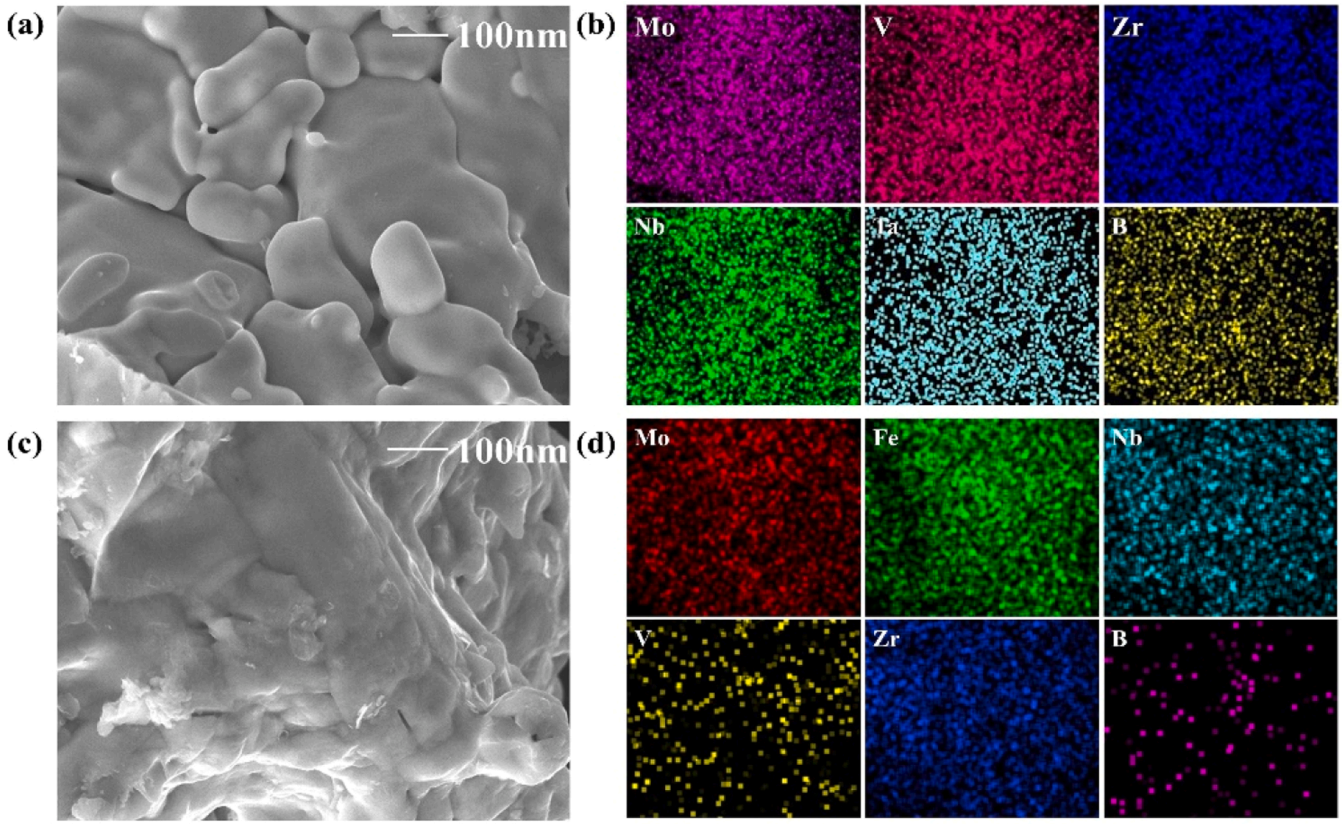

Fig. 5. STEM images of (a) $(Mo_{0.2}Zr_{0.2}V_{0.2}Nb_{0.2}Ta_{0.2})B_2$ and (c) $(Mo_{0.2}Zr_{0.2}V_{0.2}Nb_{0.2}Fe_{0.2})B_2$. EDS elemental mappings of (b) $(Mo_{0.2}Zr_{0.2}V_{0.2}Nb_{0.2}Ta_{0.2})B_2$ and (d) $(Mo_{0.2}Zr_{0.2}V_{0.2}Nb_{0.2}Fe_{0.2})B_2$.

by the interaction between electromagnetic waves and materials. After the interaction between electromagnetic waves and materials, the electromagnetic wave energy (E_I, Incident) can be decomposed into three parts: reflected electromagnetic wave energy (E_R, Reflection), transmitted electromagnetic wave energy (E_T, Transmission), and absorbed electromagnetic wave energy (E_A, Absorption) [38]. The absorbing material not only needs to reduce the E_T, but also needs to reduce the E_R as much as possible, so that the outside world is protected from the interference of the radiation source, and the radiation source itself is also protected from the interference of secondary reflection electromagnetic waves. The dissipation of EM wave energy can be carried out by electronic and/or magnetic interactions between the microwave absorber and the alternating EM wave field. Therefore, the complex permittivity ($\varepsilon_r = \varepsilon' + j\varepsilon''$) and complex permeability ($\mu_r = \mu' + j\mu''$) are the two key factors that determine the absorption performance of electromagnetic waves, with the real part (ε' and μ') and the imaginary part (ε'' and μ'') representing the storage and loss capacity of electromagnetic wave energy, respectively [34].

In order to evaluate the electromagnetic wave absorption performance of the synthetic HEB_2 powder, the frequency-dependent EM parameters are summarized in Fig. 7. As shown in Fig. 7(a), the ε' decreases with increasing frequency, which is a dispersion phenomenon. Essentially, the polarizability of a dielectric consists of several contributions to electronic, ionic, orientation, and steric charge polarization [29,39]. The relaxation frequencies of electron and ion polarization are in the frequency range of THz and PHz, respectively, and the offset of the orientation direction can be maintained with the action of the alternating electric field in the GHz range. However, space charge polarization does not contribute due to its lower relaxation frequency, while the effect of orientation polarization weakens with increasing frequency. Thus, electron and ionic bias polarization plays a dominant role in determining polarizability, while orientation and steric charge polarization contribute to dielectric losses [40]. In the case of TMB_2 compounds, the bonding between transition metal (TM) and boron (B) is characterized by both ionic and covalent interactions. The ionic component arises from the transfer of charge from the transition metal atom to the boron atom, while the covalent aspect is attributed to the hybridization of the d electrons from the transition metal and the p electrons from boron. It is observed that as one progresses from 3d to 5d TMB_2 compounds, the strength of the ionic bonding between the transition metal and boron diminishes. Consequently, the dielectric polarization capability of $(Mo_{0.2}Zr_{0.2}V_{0.2}Nb_{0.2}Fe_{0.2})B_2$ is considerably greater than that of $(Mo_{0.2}Zr_{0.2}V_{0.2}Nb_{0.2}Ta_{0.2})B_2$. Fig. 7(b) shows the frequency dependence of the virtual permittivity (ε''), which is mainly due to polarization relaxation losses and conduction losses, which can be expressed as:

$$\varepsilon'' \approx \varepsilon_p'' + \varepsilon_c'' = (\varepsilon_0 - \varepsilon_\infty)\frac{\omega\tau}{1+\omega^2\tau^2} + \frac{\sigma}{2\pi f \varepsilon_0} \quad (3)$$

Where ε_p'' and ε_c'' denote polarization and conduction losses, respectively, ε_0 and ε_∞ refer to the dielectric constant in a vacuum and at infinite frequencies, ω is the angular frequency, τ is the relaxation time, and f is the frequency. The presence of residual impurities and paraffin can stimulate interfacial polarization (known as the Maxwell-Wagner effect [28]) and associated relaxation in heterogeneous materials, which is related to the specific surface area of HE TMB_2 powder. In Fig. 7 (b), it can be seen that the ε'' of $(Mo_{0.2}Zr_{0.2}V_{0.2}Nb_{0.2}Ta_{0.2})B_2$ is relatively flat and low in the range of 1–18 GHz, and the ε'' of $(Mo_{0.2}Zr_{0.2}V_{0.2}Nb_{0.2}Fe_{0.2})B_2$ fluctuates greatly in the range of 1–18 GHz, and it can be seen that the dielectric loss capacity of the material in the frequency band above 11 GHz is strong, and the average particle size is nearly twice as different from other previous studies, and its value is much larger than the value in other studies, so it can be seen that the material mainly dissipates electromagnetic wave energy through

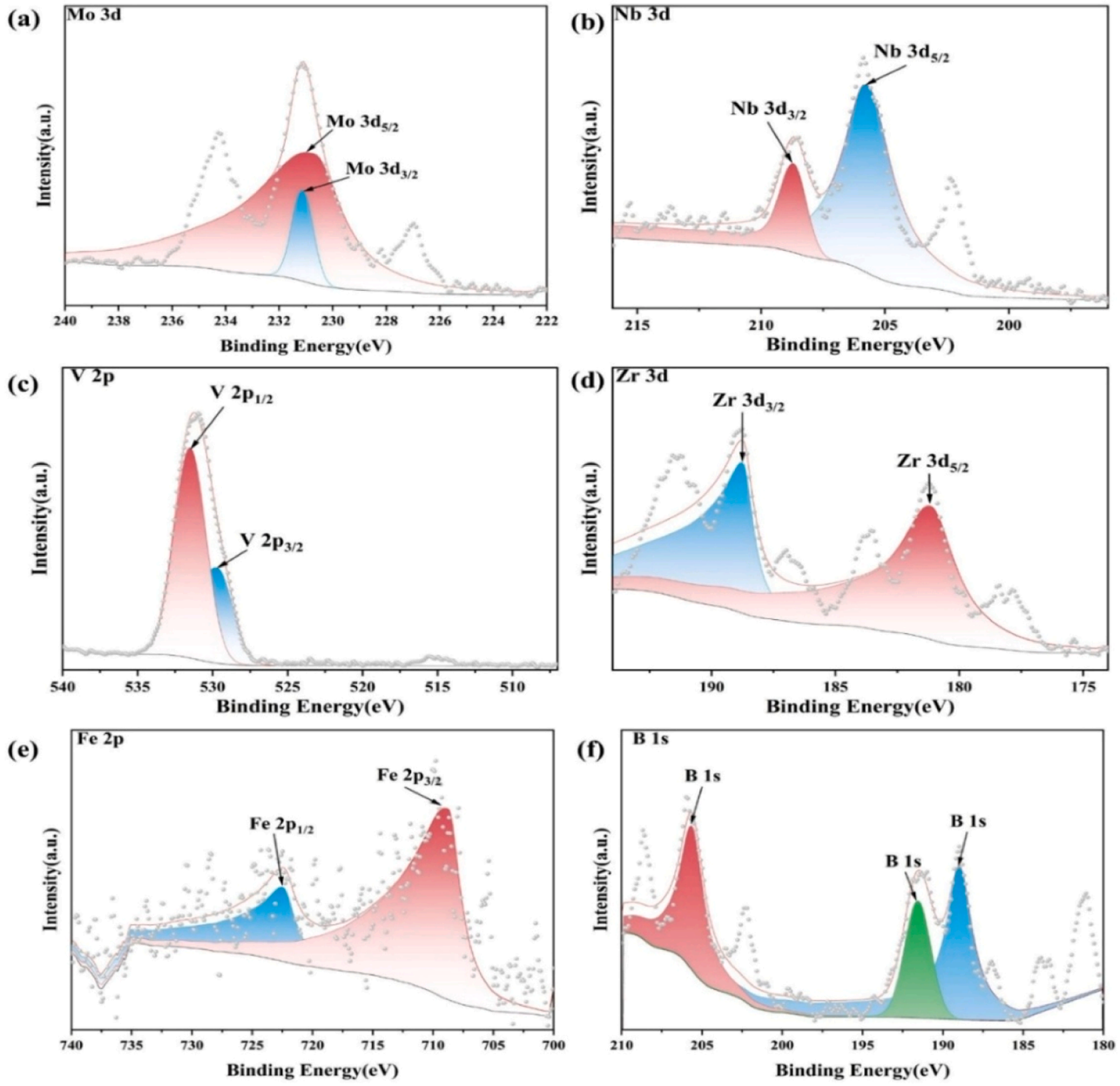

Fig. 6. High-resolution XPS spectra with peak fitting of (a) Mo 3d, (b) Nb 3d, (c) V 2p, (d) Zr 3d, (e) Fe 2p and (f) B 1 s for the as-synthesized $(Mo_{0.2}Zr_{0.2}V_{0.2}Nb_{0.2}Fe_{0.2})B_2$ high-entropy ceramic (Circles stand for experimental data and solid lines are fitting results.

polarization loss [31]. In addition, the formation of multi-principal component solid solutions is expected to introduce a large number of defects that can act as polarization centers, hindering the reorientation of the dipole and the rearrangement of space charges in the alternating electric field, resulting in energy consumption [41].

The real permeability (μ') and virtual permeability (μ'') of HE TMB_2 are shown in Fig. 7(c) and (d). In diborides, the incorporation of boron (B) atoms leads to a reduction in the atomic magnetic moment of the system; specifically, the magnetic moment (MM) value diminishes as the molar ratio of B atoms increases. This phenomenon can be attributed to the propensity of B atoms to establish nonpolar B-B covalent bonds, which possess a higher binding strength [42]. Most transition metal diborides exhibit paramagnetic behavior, while those belonging to the fourth subgroup demonstrate antiferromagnetism [43]. This antiferromagnetic characteristic influences the magnetization of high-entropy borides (HEB). Furthermore, the introduction of FeB_2, a notable ferromagnetic material, significantly impacts the magnetic storage capacity of the system. Fig. 7(c) shows that the μ' of both groups is maintained at about 1, and $(Mo_{0.2}Zr_{0.2}V_{0.2}Nb_{0.2}Fe_{0.2})B_2$ has a low magnetic susceptibility value due to the introduction of FeB_2 with ferromagnetic properties [29], which has a negative impact on the magnetic storage capacity. However, in Fig. 7(d), the value of μ'' of $(Mo_{0.2}Zr_{0.2}V_{0.2}Nb_{0.2}Fe_{0.2})B_2$ is nearly 4 times higher than that of $(Mo_{0.2}Zr_{0.2}V_{0.2}Nb_{0.2}Ta_{0.2})B_2$, and the value is larger in the low frequency band, indicating that the introduction of magnetic elements effectively increases the magnetic loss and narrows the gap between dielectric loss and magnetic loss. Therefore, the introduction of FeB_2 into HE TMB_2 avoids skin effects and enables better impedance matching at high frequencies.

Typically, the dielectric loss capability is evaluated by the dielectric loss tangent ($\tan\delta_\varepsilon = \varepsilon''/\varepsilon'$). As can be seen from Fig. 8(a), the overall value of $(Mo_{0.2}Zr_{0.2}V_{0.2}Nb_{0.2}Fe_{0.2})B_2$ is lower than that of $(Mo_{0.2}Zr_{0.2}V_{0.2}Nb_{0.2}Ta_{0.2})B_2$, indicating that the introduction of magnetic elements will cause strong lattice distortion (local stress) and stress

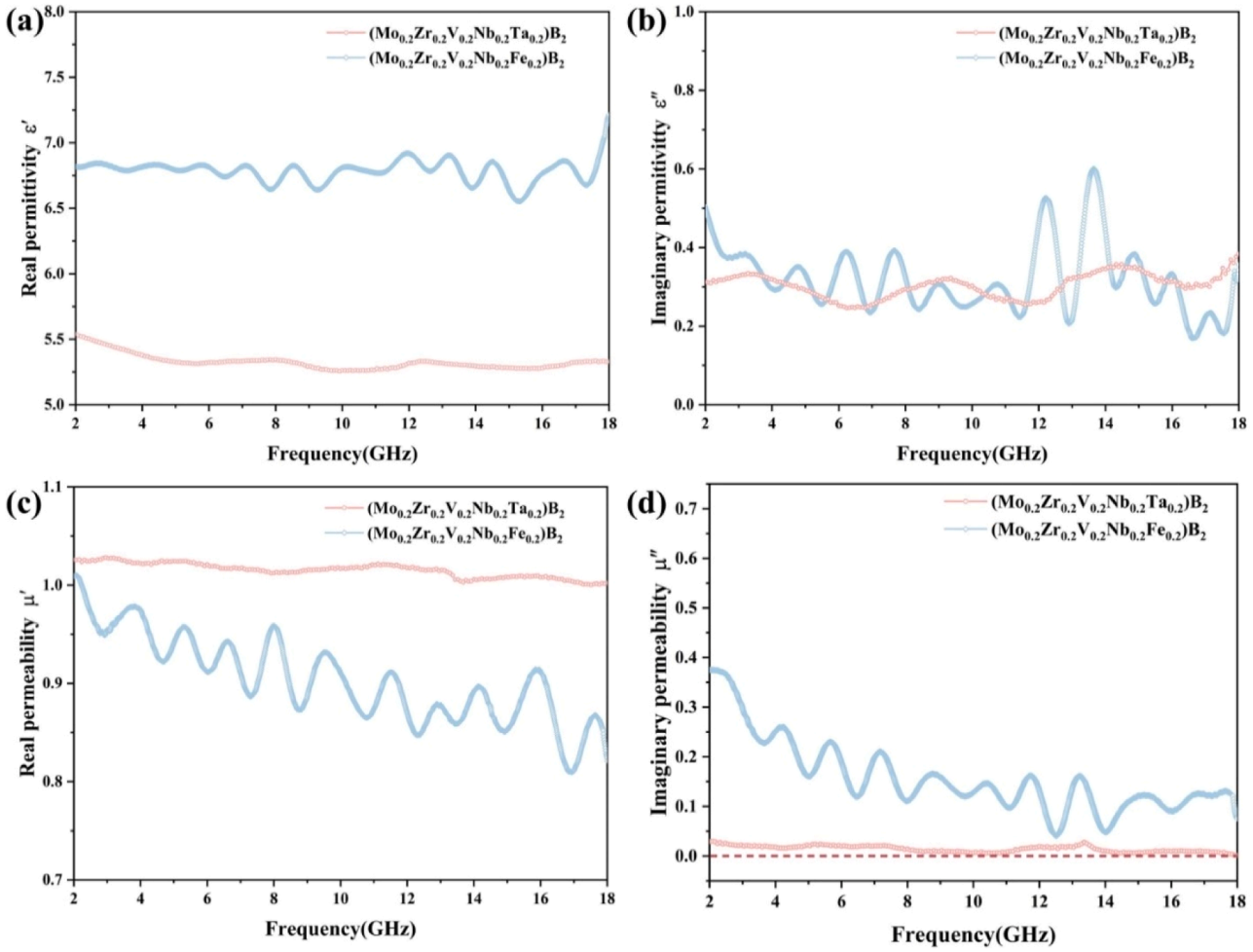

Fig. 7. Electromagnetic parameters of $(Mo_{0.2}Zr_{0.2}V_{0.2}Nb_{0.2}X_{0.2})B_2$ (X = Ta, Fe): (a) real permittivity (ε′); (b) imaginary permittivity (ε″); (c) real permeability (μ′); (d) imaginary permeability (μ″).

fluctuations in the local chemical environment of the material, which can enhance the electron scattering and reduce the electron conductivity, effectively reducing the conductivity loss. As expected, a significant resonance $\tan\delta_\mu = \mu''/\mu'$, is observed in Fig. 8(b), which can be attributed to the resonance loss. In the weak EM field in the GHz range, the electron paramagnetic resonance frequency is in the microwave frequency range, which is expected to lead to a strong attenuation of EM wave energy [41, 44]. In addition, excitation from different d-orbital energy levels also contributes to the resonant loss as a response to the incident EM wave energy [41]. Therefore, resonant and eddy current losses are the main contributors to magnetic losses, where eddy current losses are only related to the conductivity (σ) and matching thickness (d) of the material [44]. The magnetic loss tangent of $(Mo_{0.2}Zr_{0.2}V_{0.2}Nb_{0.2}Fe_{0.2})B_2$ is significantly higher than that of $(Mo_{0.2}Zr_{0.2}V_{0.2}Nb_{0.2}Ta_{0.2})B_2$, indicating that the introduction of magnetic elements can effectively improve the magnetic loss capacity of highly conductive materials and optimize impedance matching. As shown in the Fig. 8(c), the total loss tangent $(\tan\delta_\varepsilon + \tan\delta_\mu)$ of $(Mo_{0.2}Zr_{0.2}V_{0.2}Nb_{0.2}Ta_{0.2})B_2$ remains almost constant with frequency, while the total loss tangent of $(Mo_{0.2}Zr_{0.2}V_{0.2}Nb_{0.2}Fe_{0.2})B_2$ decreases with increasing frequency, which proves that the overall loss capacity of $(Mo_{0.2}Zr_{0.2}V_{0.2}Nb_{0.2}Fe_{0.2})B_2$ is significantly improved under the influence of magnetic elements and high-entropy design.

As shown in the Fig. 9(a) and (b), the Cole-Cole semicircles are present in all the samples, indicating the presence of the Debye relaxation process in the samples, and due to the non-negligible conductivity and multiple relaxation times in the HEB_2, we identified a skewed semicircle representing the relaxation process [45].These results show that there is a polarization loss in the electromagnetic field of HEB_2. After the obvious introduction of magnetic elements, $(Mo_{0.2}Zr_{0.2}V_{0.2}Nb_{0.2}Fe_{0.2})B_2$ has more Cole-Cole semicircles and a larger semicircle radius than $(Mo_{0.2}Zr_{0.2}V_{0.2}Nb_{0.2}Ta_{0.2})B_2$, indicating a higher number of polarization relaxations and a higher polarization relaxation intensity. HEB_2 has a large number of oxygen vacancies and is dipole-polarized in the electromagnetic field. The Debye relaxation process is triggered by these two polarizations. It was demonstrated that the introduction of magnetic elements can also lead to more polarization types, which further deplete electromagnetic waves. Under the weak EM field in the GHz range, the electron paramagnetic resonance frequency is in the microwave frequency range, which is expected to cause a strong attenuation of EM wave energy [11,13]. In addition, excitation from different d orbital energy levels as a response to the energy of the incident EM wave also leads to resonance losses [41,44]. Therefore, resonance losses and eddy current losses are the main contributors to magnetic losses, where eddy current losses are only related to the conductivity (σ) and matching thickness (d) of the material, as shown in Eq. (4) [34]. The type of loss can depend on the following formula:

$$C_0 = \mu''(\mu')f^{-1} = 2\pi\mu_0 d^2\sigma \tag{4}$$

where μ_0 is the vacuum permeability. Assuming that eddy current loss is the only cause of magnetic loss, the C_0 value should be kept constant. According to Fig. 8(d), it is evident that electron paramagnetic resonance loss is the predominant factor. Within the tested frequency range, the $(Mo_{0.2}Zr_{0.2}V_{0.2}Nb_{0.2}Ta_{0.2})B_2$ material exhibits minimal variation

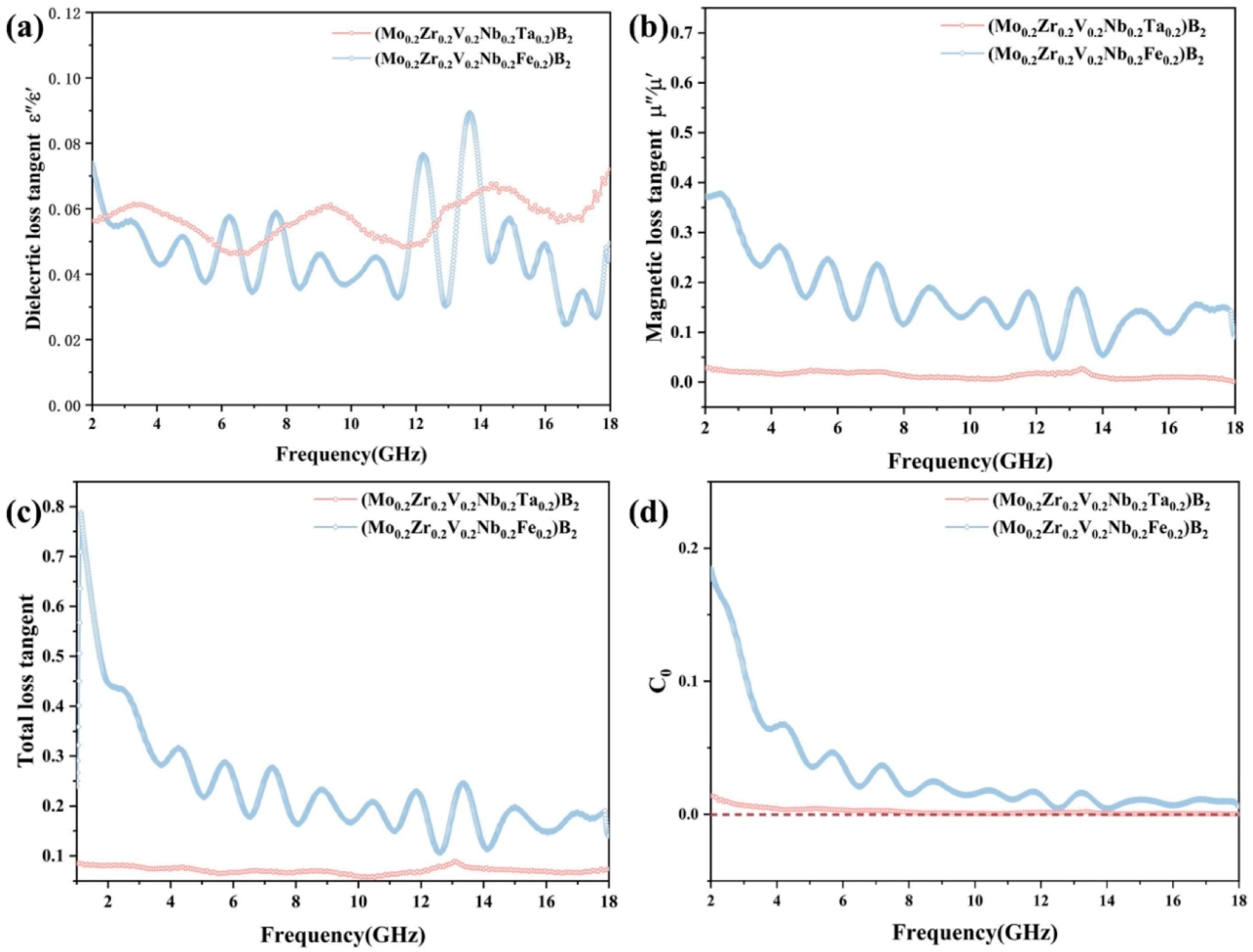

Fig. 8. Frequency dependences of (a) dielectric loss tangent(ε"/ε′); (b) magnetic loss tangent (μ''/μ'); (c) total tangent; (d) C_0–f curves.

with frequency, suggesting that only eddy current loss is influential. Conversely, the $(Mo_{0.2}Zr_{0.2}V_{0.2}Nb_{0.2}Fe_{0.2})B_2$ material demonstrates significant changes in response to frequency fluctuations within the same testing range, indicating that electron paramagnetic resonance occurs in the test range, and as can be seen from Fig. 8(b), The $(Mo_{0.2}Zr_{0.2}V_{0.2}Nb_{0.2}Fe_{0.2})B_2$ resonates at 2.5, 4.2, 5.7, 7.2, 8.8, 10.4, 11.8, 13.2, 15.0, 16.8 and 17.7 GHz, while the $(Mo_{0.2}Zr_{0.2}V_{0.2}Nb_{0.2}Ta_{0.2})B_2$ has no resonant losses. The occurrence of resonant losses in the GHz range is mainly due to the anisotropic magnetic susceptibility, the crystal field effect, and the large number of defects in HE TMB_2 caused by electron paramagnetic resonance [46]. The occurrence of resonant loss in the GHz range is mainly due to the anisotropic magnetic susceptibility of $(Mo_{0.2}Zr_{0.2}V_{0.2}Nb_{0.2}X_{0.2})B_2$ (X = Ta, Fe), the crystal field effect, and the electron paramagnetic resonance caused by a large number of defects [47]. It is proved that the introduction of magnetic elements enriches the types of magnetic losses, thereby adjusting the impedance matching. Combined with the tangent of dielectric and magnetic losses, it can be inferred that the synergistic effect of dielectric and magnetic losses is achieved in $(Mo_{0.2}Zr_{0.2}V_{0.2}Nb_{0.2}Fe_{0.2})B_2$. Taking into account the impact of double loss, the attenuation constant (α) presented in Fig. 9(c) was employed to conduct a thorough assessment of the dissipation capacity of $(Mo_{0.2}Zr_{0.2}V_{0.2}Nb_{0.2}X_{0.2})B_2$ (X = Ta, Fe).:

$$\alpha = \frac{\sqrt{2}\pi f}{c} \times \sqrt{(\mu''\varepsilon'' - \mu'\varepsilon') + \sqrt{(\mu\varepsilon - \mu'\varepsilon')^2 + (\mu'\varepsilon + \mu\varepsilon')^2}} \quad (5)$$

As shown in the Fig. 10, $(Mo_{0.2}Zr_{0.2}V_{0.2}Nb_{0.2}Fe_{0.2})B_2$ exhibits a strong frequency-dependent dissipation capability much higher than that of $(Mo_{0.2}Zr_{0.2}V_{0.2}Nb_{0.2}Ta_{0.2})B_2$, and exhibits stable and high-energy dissipation capability in the high frequency band. In order to evaluate the electromagnetic wave absorption capacity, the reflection loss (RL) is simulated using Eq. (1) as the key criterion. The minimum reflection loss (RL)of pure phase ZrB_2 is not less than −5 dB in the range of 1–5 mm and 2–18 GHz, while the effective absorption bandwidth (EAB) is 0 [26]. As shown in the figure, almost 90 % of the electromagnetic wave absorption can be achieved at different thicknesses, especially in the high frequency band (14–18 GHz), $(Mo_{0.2}Zr_{0.2}V_{0.2}Nb_{0.2}X_{0.2})B_2$ (X = Ta, Fe) can achieve almost full band coverage absorption capacity. Among them, the HE TMB_2 with a thickness of 6.0 mm can achieve a minimum reflection loss (RL_{min}) of −33.1 dB (15.4 GHz). It is proved that through the high-entropy design and the introduction of magnetic elements, the magnetic loss can be increased while maintaining high dielectric loss by enriching the polarization type, so that the electromagnetic wave can be absorbed by the internal loss of the material. It can effectively control the electromagnetic loss balance of highly conductive absorbing materials, so as to optimize the impedance matching and overcome the bottleneck that electromagnetic waves cannot enter the highly conductive ceramic materials. From the above analysis, it can be seen that by designing $(Mo_{0.2}Zr_{0.2}V_{0.2}Nb_{0.2}X_{0.2})B_2$ (X = Ta, Fe) to customize the impedance matching, a strong broadband absorption capacity can be achieved, that is, the dielectric loss can be adjusted by reducing the conductivity, and the magnetic loss can be enhanced by adding a component with more magnetic field energy dissipation paths.

As show in Fig. 11, due to the synergistic effect of reduced conductivity and increased magnetic loss, the goal of balancing the dielectric loss and magnetic loss in the tuned single-phase HEB_2 is achieved,

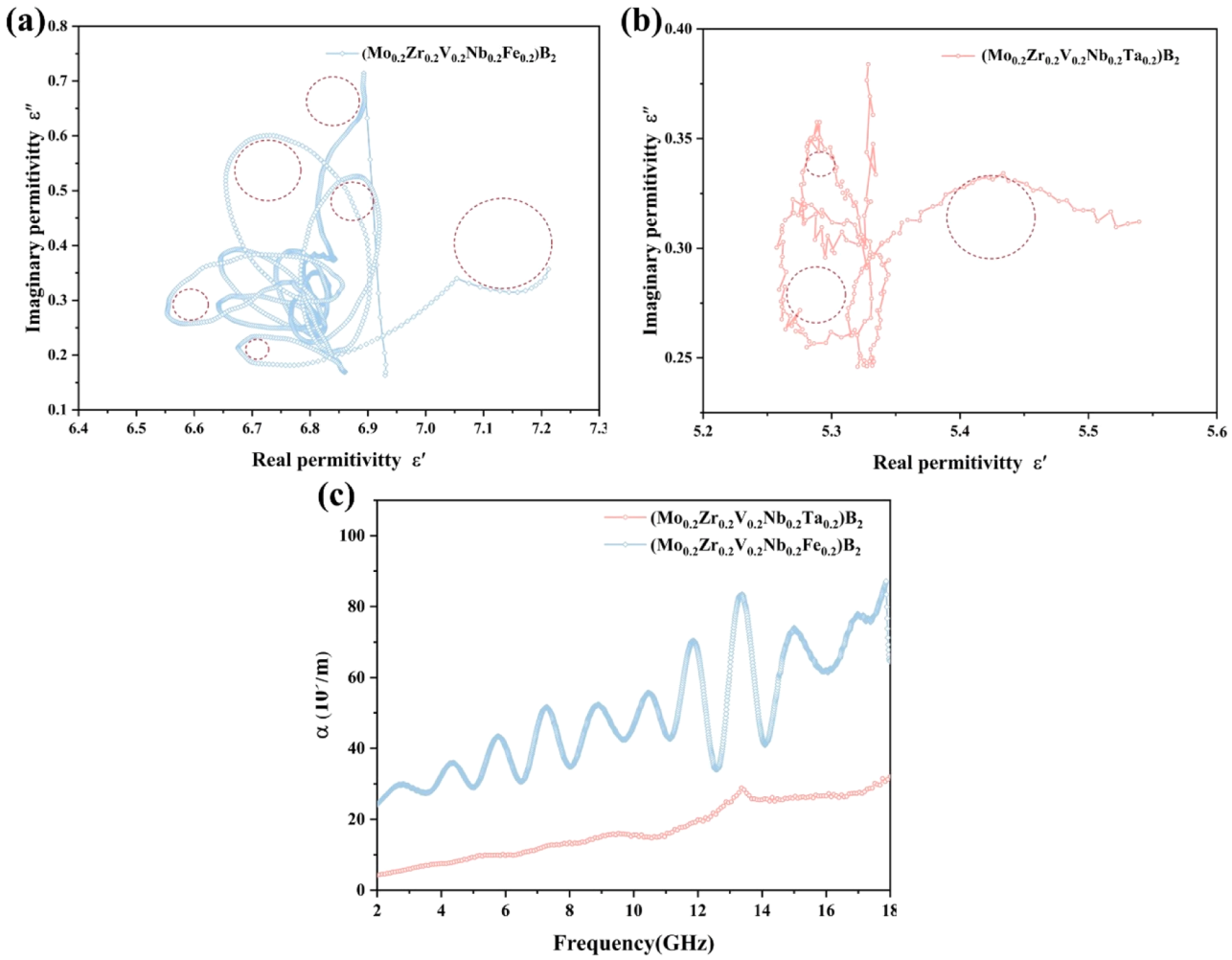

Fig. 9. (a-b) Cole–Cole semicircles (ε''—ε') and (c) Frequency dependences of attenuation constant (α) of $(Mo_{0.2}Zr_{0.2}V_{0.2}Nb_{0.2}X_{0.2})B_2$ (X = Ta, Fe).

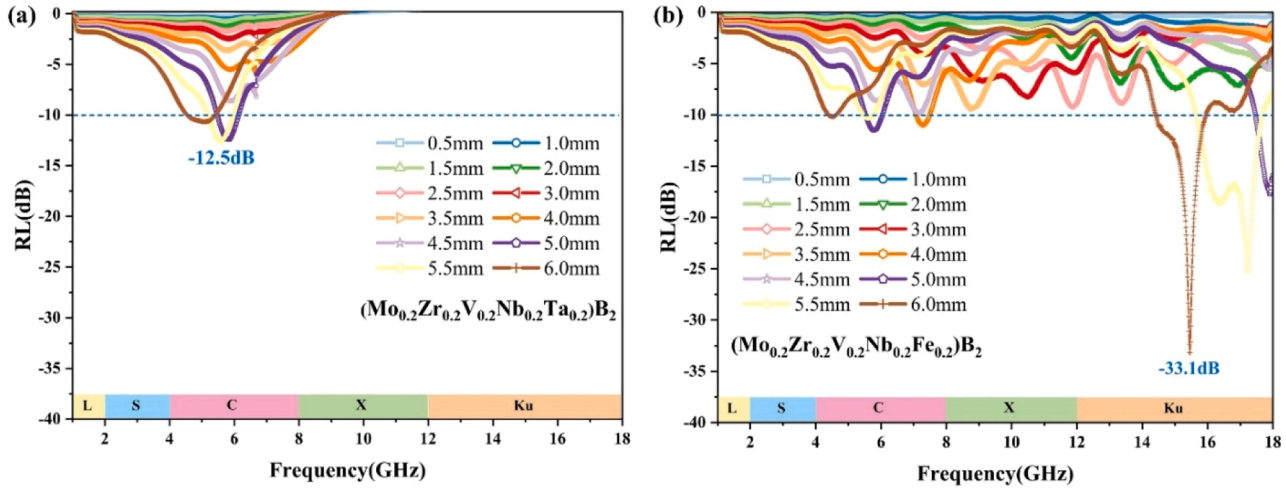

Fig. 10. Frequency dependences of RL values of (a) $(Mo_{0.2}Zr_{0.2}V_{0.2}Nb_{0.2}Ta_{0.2})B_2$, (b) $(Mo_{0.2}Zr_{0.2}V_{0.2}Nb_{0.2}Fe_{0.2})B_2$.

leading to good electromagnetic wave absorption performance. The material exhibits favorable electrical conductivity, as the presence of free electrons allows for the absorption of electromagnetic (EM) energy during exposure to electromagnetic wave radiation. This process facilitates an increase in EM energy consumption through the migration of electrons within the material system [48]. And due to the introduction of FeB_2 with ferromagnetic properties, it leads to the synergistic effect of electron paramagnetic resonance loss and eddy current loss, which improves the magnetic loss; at the same time, it increases the number of polarization relaxation times, enhances the strength of polarization relaxation and, under the influence of a large number of boron vacancies, dipole polarization occurs, which results in a better depletion of

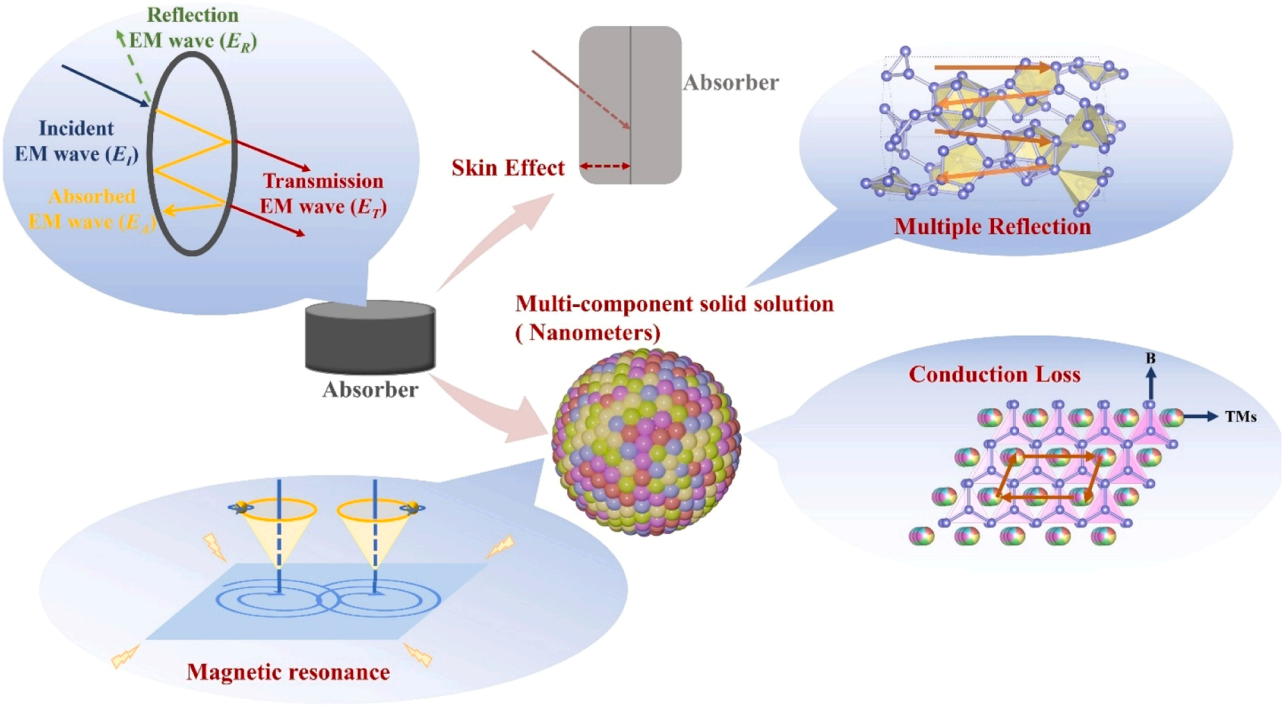

Fig. 11. Mechanism of electromagnetic wave absorption in high-entropy diborides.

electromagnetic waves, effectively tuning the balance of electromagnetic loss in the high-conductivity absorbing material, thus optimizing the impedance matching, which leads to a good electromagnetic wave absorption performance, to overcome the bottleneck of electromagnetic waves cannot enter the high-conductivity ceramic-like materials.

4. Conclusion

In summary, we successfully synthesized two novel high-entropy diborides, specifically $(Mo_{0.2}Zr_{0.2}V_{0.2}Nb_{0.2}X_{0.2})B_2$ (X = Ta, Fe), utilizing a rapid Joule heating apparatus at a temperature of 1900 °C for a duration of 10 minutes. Among these compounds, the nonmagnetic variant, $(Mo_{0.2}Zr_{0.2}V_{0.2}Nb_{0.2}Ta_{0.2})B_2$, demonstrates suboptimal electromagnetic wave absorption characteristics, with a minimum reflection loss of merely −12.5 dB at a frequency of 5.7 GHz and a thickness of 5.5 mm. Conversely, the magnetic variant, $(Mo_{0.2}Zr_{0.2}V_{0.2}Nb_{0.2}Fe_{0.2})B_2$, exhibited superior electromagnetic wave absorption capabilities, achieving a minimum reflection loss of −33.15 dB at 15.4 GHz with a thickness of 6.0 mm. Analysis of the electromagnetic parameters indicated that the incorporation of the magnetic element (Fe) significantly enhances both the permittivity and permeability of the $(Mo_{0.2}Zr_{0.2}V_{0.2}Nb_{0.2}X_{0.2})B_2$ material, thereby optimizing its impedance matching and facilitating the efficient absorption of electromagnetic waves. Furthermore, the "cocktail effect" arising from the presence of various elements within the high-entropy system contributed to the development of lattice distortions and defects, which serve as polarization centers within the solid solution, further augmenting the material's electromagnetic wave absorption capabilities. This research offered valuable insights for the advancement of effective electromagnetic wave absorbing materials.

CRediT authorship contribution statement

Shuyi Zeng: Conceptualization; Data curation; Visualization; Formal analysis; Investigation; Writing–original draft. **Qingyun Chen:** Funding acquisition; Writing–review & editing. **Qijie Chen:** Data curation. **Xingye Wang:** Supervision. **Peng Sun:** Funding acquisition; Supervision. **Chencheng Liu:** Data curation; Writing–review & editing. **Tong Zhu:** Formal analysis. **Yi Zhu:** Supervision. **Wenlong Zhang:** Investigation. **Yuezhong Wang:** Funding acquisition; Investigation. **Nan Jiang:** Visualization.

Declaration of Competing Interest

The authors declare that they have no known competing financial interests or personal relationships that could have appeared to influence the work reported in this paper.

Acknowledgments

This work was supported by Guangxi Natural Science Foundation (2022GXNSFAA035527), the Natural Science Foundation of Tianjin (23JCZDJC00150, 22JCZDJC00080), Science and Technology Major Project of Ningbo (2021Z123), Yongjiang Talent Introduction Programme (2021A-108-G), Youth Fund of the Chinese Academy of Sciences (JCPYJJ-22030), and Guilin University of Technology Research Startup Fund (RD2100000621).

Data Availability

Data will be made available on request.

References

[1] M.A. Jamshed, F. Heliot, T.W.C. Brown, A survey on electromagnetic risk assessment and evaluation mechanism for future wireless communication systems, IEEE J. Electromagn., RF Microw. Med. Biol. 4 (1) (2020) 24–36, https://doi.org/10.1109/jerm.2019.2917766.
[2] M. Green, X. Chen, Recent progress of nanomaterials for microwave absorption, J. Mater. 5 (4) (2019) 503–541, https://doi.org/10.1016/j.jmat.2019.07.003.
[3] H. Pang, Y. Duan, L. Huang, L. Song, J. Liu, T. Zhang, X. Yang, J. Liu, X. Ma, J. Di, X. Liu, Research advances in composition, structure and mechanisms of microwave absorbing materials, Compos. Part B: Eng. 224 (2021), https://doi.org/10.1016/j.compositesb.2021.109173.
[4] C. Wang, V. Murugadoss, J. Kong, Z. He, X. Mai, Q. Shao, Y. Chen, L. Guo, C. Liu, S. Angaiah, Z. Guo, Overview of carbon nanostructures and nanocomposites for electromagnetic wave shielding, Carbon 140 (2018) 696–733, https://doi.org/10.1016/j.carbon.2018.09.006.

[5] Y. Wang, F. Luo, P. Wei, W. Zhou, D. Zhu, Enhanced dielectric properties and high-temperature microwave absorption performance of Zn-doped Al_2O_3 ceramic, J. Electron. Mater. 44 (7) (2015) 2353–2358, https://doi.org/10.1007/s11664-015-3787-4.

[6] H.O. Pierson, Handbook of Refractory Carbides & Nitrides: Properties, Characteristics, Processing and Applications, William Andrew, 1996.

[7] K.E. Spear, Phase behavior and related properties of rare earth borides, Phase Diagr. Mater. Sci. Technol. 4 (1976) 91–159, https://doi.org/10.1016/B978-0-12-053204-9.50010-2.

[8] Y. Pan, C. Jing, Influence of vacancies on the mechanical and thermodynamic properties of TM_2B_3(TM=Ru and Os) borides from first-principles calculations, Ceram. Int. 45 (17) (2019) 21373–21378, https://doi.org/10.1016/j.ceramint.2019.07.124.

[9] Y. Pan, J. Zhu, Enhancing the Vickers hardness of Yttrium borides through bond optimization, Mater. Today Commun. 38 (2024), https://doi.org/10.1016/j.mtcomm.2024.108428.

[10] Y. Pan, D. Pu, G. Liu, P. Wang, Influence of alloying elements on the structural stability, elastic, hardness and thermodynamic properties of Mo5SiB2 from first-principles calculations, Ceram. Int. 46 (10) (2020) 16605–16611, https://doi.org/10.1016/j.ceramint.2020.03.233.

[11] H.J. Juretschke, R. Steinitz, Hall effect and electrical conductivity of transition-metal diborides, J. Phys. Chem. Solids 4 (1) (1958) 118–127, https://doi.org/10.1016/0022-3697(58)90201-4.

[12] P. Vajeeston, P. Ravindran, C. Ravi, R. Asokamani, Electronic structure, bonding, and ground-state properties of AlB_2type transition-metal diborides, Phys. Rev. B 63 (4) (2001) 045115, https://doi.org/10.1103/PhysRevB.63.045115.

[13] P.S. Neelakanta, Handbook of electromagnetic materials: monolithic and composite versions and their applications, CRC press, 1995.

[14] W. Zhang, X. Zhang, Q. Zhu, Y. Zheng, L.F. Liotta, H. Wu, High-efficiency and wide-bandwidth microwave absorbers based on MoS2-coated carbon fiber, J. Colloid Interface Sci. 586 (2021) 457–468, https://doi.org/10.1016/j.jcis.2020.10.109.

[15] X. Qi, J. Xu, Q. Hu, Y. Deng, R. Xie, Y. Jiang, W. Zhong, Y. Du, Metal-free carbon nanotubes: synthesis, and enhanced intrinsic microwave absorption properties, Sci. Rep. 6 (1) (2016) 28310, https://doi.org/10.1038/srep28310.

[16] C.M. Rost, E. Sachet, T. Borman, A. Moballegh, E.C. Dickey, D. Hou, J.L. Jones, S. Curtarolo, J.-P. Maria, Entropy-stabilized oxides, Nat. Commun. 6 (1) (2015), https://doi.org/10.1038/ncomms9485.

[17] J. Zhou, J. Zhang, F. Zhang, B. Niu, L. Lei, W. Wang, High-entropy carbide: a novel class of multicomponent ceramics, Ceram. Int. 44 (17) (2018) 22014–22018, https://doi.org/10.1016/j.ceramint.2018.08.100.

[18] Y. Dong, K. Ren, Y. Lu, Q. Wang, J. Liu, Y. Wang, High-entropy environmental barrier coating for the ceramic matrix composites, J. Eur. Ceram. Soc. 39 (7) (2019) 2574–2579, https://doi.org/10.1016/j.jeurceramsoc.2019.02.022.

[19] A. Sarkar, C. Loho, L. Velasco, T. Thomas, S.S. Bhattacharya, H. Hahn, R. Djenadic, Multicomponent equiatomic rare earth oxides with a narrow band gap and associated praseodymium multivalency, Dalton Trans. 46 (36) (2017) 12167–12176, https://doi.org/10.1039/c7dt02077e.

[20] H. Zhang, B. Zhao, F.-Z. Dai, H. Xiang, Z. Zhang, Y. Zhou, $Cr_{0.2}Mn_{0.2}Fe_{0.2}Co_{0.2}Mo_{0.2}$)B: A novel high-entropy monoboride with good electromagnetic interference shielding performance in K-band, J. Mater. Sci. Technol. 77 (2021) 58–65, https://doi.org/10.1016/j.jmst.2020.09.047.

[21] D. Bérardan, S. Franger, D. Dragoe, A.K. Meena, N. Dragoe, Colossal dielectric constant in high entropy oxides, physica status solidi (RRL), Rapid Res. Lett. 10 (4) (2016) 328–333, https://doi.org/10.1002/pssr.201600043.

[22] A. Sarkar, L. Velasco, D. Wang, Q. Wang, G. Talasila, L. de Biasi, C. Kübel, T. Brezesinski, S.S. Bhattacharya, H. Hahn, B. Breitung, High entropy oxides for reversible energy storage, Nat. Commun. 9 (1) (2018), https://doi.org/10.1038/s41467-018-05774-5.

[23] R. Witte, A. Sarkar, L. Velasco, R. Kruk, R.A. Brand, B. Eggert, K. Ollefs, E. Weschke, H. Wende, H. Hahn, Magnetic properties of rare-earth and transition metal based perovskite type high entropy oxides, J. Appl. Phys. 127 (18) (2020), https://doi.org/10.1063/5.0004125.

[24] L. Qiao, J. Bi, G. Liang, C. Liu, Z. Yin, Y. Yang, H. Wang, S. Wang, M. Shang, W. Wang, Synthesis and electromagnetic wave absorption performances of a novel $(Mo_{0.25}Cr_{0.25}Ti_{0.25}V_{0.25})_3AlC_2$ high-entropy MAX phase, J. Mater. Sci. Technol. 137 (2023) 112–122, https://doi.org/10.1016/j.jmst.2022.07.039.

[25] J. Zhang, W. Wang, Z. Zhang, J. Chen, X. Sun, G. Sun, Y. Liang, G. Han, W. Zhang, Synthesis, microstructure and electromagnetic wave absorption properties of high-entropy carbide powders, J. Alloy. Compd. 966 (2023) 171593, https://doi.org/10.1016/j.jallcom.2023.171593.

[26] X. Jian, W. Tian, J. Li, L. Deng, Z. Zhou, L. Zhang, H. Lu, L. Yin, N. Mahmood, High-Temperature Oxidation-Resistant $ZrN_{0.4}B_{0.6}$/SiC Nanohybrid for Enhanced Microwave Absorption, ACS Appl. Mater. Interfaces 11 (17) (2019) 15869–15880, https://doi.org/10.1021/acsami.8b22448.

[27] R.J. Tilley, Understanding Solids: the Science of Materials, John Wiley & Sons, 2004.

[28] L.K.H. Van Beek, The Maxwell-Wagner-Sillars effect, describing apparent dielectric loss in inhomogeneous media, Physica 26 (1) (1960) 66–68, https://doi.org/10.1016/0031-8914(60)90115-4.

[29] W. Zhang, F.-Z. Dai, H. Xiang, B. Zhao, X. Wang, N. Ni, R. Karre, S. Wu, Y. Zhou, Enabling highly efficient and broadband electromagnetic wave absorption by tuning impedance match in high-entropy transition metal diborides (HE TMB_2), J. Adv. Ceram. 10 (6) (2021) 1299–1316, https://doi.org/10.1007/s40145-021-0505-y.

[30] N. Gao, W.-P. Li, W.-S. Wang, D.-P. Liu, Y.-M. Cui, L. Guo, G.-S. Wang, Balancing dielectric loss and magnetic loss in Fe–NiS2/NiS/PVDF composites toward strong microwave reflection loss, ACS Appl. Mater. Interfaces 12 (12) (2020) 14416–14424, https://doi.org/10.1021/acsami.9b23379.

[31] W. Zhang, B. Zhao, N. Ni, H. Xiang, F.-Z. Dai, S. Wu, Y. Zhou, High entropy rare earth hexaborides/tetraborides (HE REB6/HE REB4) composite powders with enhanced electromagnetic wave absorption performance, J. Mater. Sci. Technol. 87 (2021) 155–166, https://doi.org/10.1016/j.jmst.2021.01.059.

[32] G. Tallarita, R. Licheri, S. Garroni, R. Orrù, G. Cao, Novel processing route for the fabrication of bulk high-entropy metal diborides, Scr. Mater. 158 (2019) 100–104, https://doi.org/10.1016/j.scriptamat.2018.08.039.

[33] D. Liu, T. Wen, B. Ye, Y. Chu, Synthesis of superfine high-entropy metal diboride powders, Scr. Mater. 167 (2019) 110–114, https://doi.org/10.1016/j.scriptamat.2019.03.038.

[34] P.A. Miles, W.B. Westphal, A. Von Hippel, Dielectric Spectroscopy of Ferromagnetic Semiconductors, Rev. Mod. Phys. 29 (3) (1957) 279–307, https://doi.org/10.1103/RevModPhys.29.279.

[35] R.D. Shannon, Revised effective ionic radii and systematic studies of interatomic distances in halides and chalcogenides, Acta Crystallogr. Sect. A 32 (5) (1976) 751–767, https://doi.org/10.1107/s0567739476001551.

[36] J. Li, G. Shao, Y. Ma, X. Zhao, H. Wang, R. Zhang, Processing and properties of polycrystalline cubic boron nitride reinforced by SiC whiskers, Int. J. Appl. Ceram. Technol. 16 (1) (2019) 32–38, https://doi.org/10.1111/ijac.13077.

[37] A.A. Abdel-Hamid, S. Hamar-Thibault, R. Hamar, Crystal morphology of the compound TiB2, J. Cryst. Growth 71 (3) (1985) 744–750, https://doi.org/10.1016/0022-0248(85)90386-0.

[38] W. Zhang, H. Xiang, F. Dai, Z. Sun, Y. Zhou, High-entropy ceramics: a new strategy for electromagnetic wave absorbing materials, ATERIALS Technol. 52 (2) (2022) 13–25, https://doi.org/10.12044/j.issn.1007-2330.2022.02.002.

[39] S. Li, W. Han, K. Lu, K. Ma, Y. Ma, T. Lu, Y. Ye, J. Qi, Highly transparent $Sm_2Zr_2O_7$ ceramics with excellent dielectric performance, Appl. Phys. Lett. 123 (4) (2023) 041904, https://doi.org/10.1063/5.0155111.

[40] W. Zhang, B. Zhao, H. Xiang, F.-Z. Dai, S. Wu, Y. Zhou, One-step synthesis and electromagnetic absorption properties of high entropy rare earth hexaborides (HE REB_6) and high entropy rare earth hexaborides/borates (HE REB_6/HE $REBO_3$) composite powders, J. Adv. Ceram. 10 (1) (2020) 62–77, https://doi.org/10.1007/s40145-020-0417-2.

[41] Mabbs, F.E., Collison, D., Electron paramagnetic resonance of d transition metal compounds. (1992).

[42] L. Hui, Z. Xie, C. Li, Z.-Q. Chen, FeX (X = B, N) binary compounds: First-principles calculations of electronic structures, theoretic hardness and magnetic properties, J. Magn. Magn. Mater. 451 (2018) 761–769, https://doi.org/10.1016/j.jmmm.2017.12.011.

[43] G.E. Grechnev, A.V. Fedorchenko, A.V. Logosha, A.S. Panfilov, I.V. Svechkarev, V. B. Filippov, A.B. Lyashchenko, A.V. Evdokimova, Electronic structure and magnetic properties of transition metal diborides, J. Alloy. Compd. 481 (1) (2009) 75–80, https://doi.org/10.1016/j.jallcom.2009.03.123.

[44] T. Kolodiazhnyi, A. Petric, Analysis of point defects in polycrystalline $BaTiO_3$ by electron paramagnetic resonance, J. Phys. Chem. Solids 64 (6) (2003) 953–960, https://doi.org/10.1016/s0022-3697(02)00454-7.

[45] Y. Zhou, B. Zhao, H. Chen, H. Xiang, F.-Z. Dai, S. Wu, W. Xu, Electromagnetic wave absorbing properties of TMCs (TM=Ti, Zr, Hf, Nb and Ta) and high entropy $(Ti_{0.2}Zr_{0.2}Hf_{0.2}Nb_{0.2}Ta_{0.2})C$, J. Mater. Sci. Technol. 74 (2021) 105–118, https://doi.org/10.1016/j.jmst.2020.10.016.

[46] N. Luo, K. Han, M.J. Cabral, X. Liao, S. Zhang, C. Liao, G. Zhang, X. Chen, Q. Feng, J.-F. Li, Y. Wei, Constructing phase boundary in $AgNbO_3$ antiferroelectrics: pathway simultaneously achieving high energy density and efficiency, Nat. Commun. 11 (1) (2020) 4824, https://doi.org/10.1038/s41467-020-18665-5.

[47] H. Chen, B. Zhao, Z. Zhao, H. Xiang, F.-Z. Dai, J. Liu, Y. Zhou, Achieving strong microwave absorption capability and wide absorption bandwidth through a combination of high entropy rare earth silicide carbides/rare earth oxides, J. Mater. Sci. Technol. 47 (2020) 216–222, https://doi.org/10.1016/j.jmst.2020.02.015.

[48] C. Liu, Q. Chen, P. Sun, X. Wang, S. Zeng, Q. Chen, T. Zhu, Y. Zhu, W. Zhang, H. Song, Y. Wang, K. Nishimura, H. Liu, N. Jiang, Synthesis of novel high-entropy diborides with high-efficiency electromagnetic wave absorption and excellent thermal stability, J. Adv. Ceram. (2025), https://doi.org/10.26599/jac.2025.9221030.